

# Large Eddy Simulations of the Effects of EMBr and SEN Submergence Depth on Turbulent Flow in the Mold Region of a Steel Caster



KAI JIN, SURYA P. VANKA, and BRIAN G. THOMAS

Transient turbulent flow in the mold region during continuous casting of steel is related to many quality problems, such as surface defects and slag entrainment. This work applies an efficient multi-GPU based code, CUFlow, to perform large eddy simulations (LES) of the turbulent flow in a domain that includes the slide gate, SEN, and mold region. The computations were first validated by comparing the predicted surface velocity with plant measurements. Then, seven LES simulations were conducted to study the effects of casting speed, electromagnetic braking (EMBr) field strength, and submerged entry nozzle (SEN) depth on the transient flow. The results show that EMBr has an important influence on flow inside the SEN, in addition to flow in the mold. With EMBr, an “M-shaped” flow profile is seen inside the SEN. The swirling flow behavior in the SEN and ports is more symmetrical at high casting speed and with higher EMBr strength. The position of the SEN ports relative to the peak magnetic field affects the EMBr performance. The results confirm and quantify how applying EMBr greatly lowers both the magnitude and turbulent variations of the surface velocity and level profile.

DOI: 10.1007/s11663-016-0801-z

© The Minerals, Metals & Materials Society and ASM International 2016

## I. INTRODUCTION

CONTINUOUS casting produces over 95 pct of steel in the world today,<sup>[1]</sup> hence even small improvements to this important industrial process can have large economic impact. The characteristics of turbulent flow in the mold region of the caster influences the creation of surface defects, slag entrainment, and other issues related to the quality of steel. The velocity across the top surface of the mold is an important parameter affecting defect formation. A very small velocity causes reduced heat transfer and leads to hook formation, meniscus freezing, and other surface defects. On the other hand, if the top surface velocity is too large, the resulting turbulence and shear layer instability may entrain slag and form inclusions in the final product. Therefore, it is very important to choose operating conditions which produce flow patterns within an optimal operational window to avoid these problems. These operating conditions include the mold cross section, casting speed, submergence depth, argon gas injection, and electromagnetic forces. The use of

electromagnetic force is an attractive method to dynamically control the mold flow due to its easy implementation by simply changing the electric current in the coils of the device.

The electromagnetic forces are commonly generated by applying a magnetic field near the mold region. A static magnetic field is attained by passing direct current (DC) through electromagnets, which induces a Lorentz force field that acts against the flow. Thus this concept is usually referred to as an electromagnetic braking (EMBr) system. Based on the DC electromagnets shape and location, there are three typical types of static magnetic field configurations: local,<sup>[2–7]</sup> single ruler<sup>[7–12]</sup> and double ruler.<sup>[12–17]</sup> The difference between these configurations as well as the use of moving magnetic fields are discussed elsewhere.<sup>[18]</sup> In this work, we focus on the double-ruler configuration which is widely used in industry and commonly known as the flow control mold (ABB Automation Technologies).<sup>[19]</sup> In the double-ruler configuration, two rectangular magnetic fields across the entire mold width are generated, with one positioned near the meniscus and the other below the nozzle ports.<sup>[13–18]</sup> This configuration is able to slow down<sup>[13,17]</sup> or to speed up<sup>[12,16]</sup> surface velocities in the mold region, and has been reported to decrease high-frequency turbulent fluctuations<sup>[12]</sup> and to improve meniscus stability.<sup>[16,17]</sup>

Owing to the hostile environment of the hot molten steel and the large number of design and operating variables which affect the process, it is difficult to optimize flow in continuous casting through measurements in real casters. Thus, computational models, water models<sup>[15]</sup> and physical models<sup>[7,8,11–14,20,21]</sup> with conducting fluids (*e.g.*, GaInSn,<sup>[8,11,12,20,21]</sup> tin,<sup>[14]</sup> and

KAI JIN, Graduate Student and Research Assistant, and SURYA P. VANKA, Research Professor, Professor Emeritus, are with the Department of Mechanical Science and Engineering, University of Illinois at Urbana–Champaign, 1206 West Green Street (MC-244), Urbana, IL, 61801. BRIAN G. THOMAS, formerly Research Professor, C.J. Gauthier Professor Emeritus with the Department of Mechanical Science and Engineering, University of Illinois at Urbana–Champaign, is now Professor with the Department of Mechanical Engineering, Colorado School of Mines, 1610 Illinois Street, Golden, CO. Contact email: bgthomas@illinois.edu

Manuscript submitted July 1, 2016.

Article published online September 9, 2016.

mercury<sup>[7,13]</sup>) are used to help understand the process. Due to the rapid development of computer hardware, computational models are widely used<sup>[2–17]</sup> as tools to understand the physical phenomena, improve, optimize, and control the process. Most computational models use the Reynolds-Averaged Navier–Stokes (RANS) approach and solve equations for the mean flow behavior.<sup>[2,4–6,8,10,13,14,17]</sup> Only a limited number of researchers have so far studied the transient behavior of the turbulent flow using well-resolved<sup>[9,16]</sup> large eddy simulations (LES) with EMBr<sup>[7,9,11,12,15,16]</sup> or without EMBr.<sup>[22]</sup>

The effects of the double-ruler EMBr system on the mean flow field in real commercial casters have been studied by several researchers. Early in 1993, Idogawa *et al.*<sup>[13]</sup> applied the RANS method to model experiments with mercury and showed that the double-ruler system can reduce the mean velocity near the meniscus and the narrow face (NF). A RANS simulation of molten tin experiments indicated that the double-ruler system with a maximum magnetic field of around 0.3 T can effectively reduce the flow velocity in the bulk but can also cause very low velocities (around 0.032 m/s) at meniscus region.<sup>[14]</sup> Using the  $k$ - $\epsilon$  RANS model, Cho *et al.*<sup>[17]</sup> showed that the EMBr can stabilize the top surface by reducing surface level fluctuations by 50 pct.

As the transient flow behavior in the caster mold is quite important,<sup>[23]</sup> several researchers have recently conducted transient LES simulations. Qian *et al.*<sup>[9]</sup> showed the formation of transient unsymmetrical vortices even if the nozzle was placed at the center of the mold. They also found that the unsymmetrical upward recirculating flow in the mold can cause unsymmetrical surface flow and generate biased vortical flows on the top surface. However, a single ruler magnet at the meniscus was seen to suppress this vortex flow. Singh *et al.*<sup>[16]</sup> studied flow in a steel caster with a double-ruler EMBr (max magnetic field 0.28 T), and showed that the EMBr makes the top surface flow more stable resulting in only small-level fluctuations. The surface velocity was reduced from 0.6 to ~0.1 m/s. Recently, a vertical electromagnetic brake system has been proposed and studied.<sup>[24]</sup> In this system, two long vertical electromagnets are placed close to the NF and a steady magnetic field is passed through the thickness of the mold. In addition to reducing the surface velocity, this configuration also reduces the impact of the steel jet on the NF.<sup>[24]</sup>

Accurate flow computations with electromagnetics can be challenging. Including the solid shell in the calculation has the effect of stabilizing the flow in the mold.<sup>[11,12]</sup> Chaudhary *et al.*<sup>[12]</sup> performed LES of a GaInSn model with single ruler and double-ruler EMBr arrangements. Their study assumed the shell to be an electrically insulated wall. This led to the observations of a transient low-frequency large-scale oscillation in the mold and an unstable flow. Singh *et al.*<sup>[11]</sup> modified this model of Chaudhary *et al.*<sup>[12]</sup> by adding an electrically conducting shell. Their LES results showed that the conducting wall can help stabilize the flow and the unsteady low-frequency oscillation flow seen previously<sup>[12]</sup> can be suppressed.

All of the above studies showed that the magnetic field affects the time-mean flow behavior in the caster as well as the transient flow structure in the mold.<sup>[11,12,16,17]</sup> It reduces the mean surface velocity and fluctuations.<sup>[9–14,16,17]</sup> However, electromagnetic forces can also generate undesired effects if not used correctly in conjunction with other casting parameters (such as submergence depth).<sup>[18]</sup> Thomas *et al.*<sup>[18]</sup> investigated the combined effects of the local EMBr system and different submergence depths on the time-mean flow using the RANS approach. Their results showed that even with same EMBr configuration, different submergence depths may considerably change the effectiveness of the braking system. However, less attention was paid to the combined effects of submergence depth and EMBr for the widely used double-ruler system. Most work was focused on the effect of EMBr on steel flow in mold region without including the full SEN.<sup>[7–15,22,24]</sup>

Although a few researchers have included the SEN in the computational domain, the magnetic field above the steel–slag interface was ignored.<sup>[16]</sup> However, simulations with RANS have shown that a strong magnetic field modifies the mean flow also inside the SEN and reduces its turbulent kinetic energy.<sup>[17]</sup> Therefore, it is clear that the transient simulations must include the effects of the magnetic field on the nozzle flow.

In the present work, we have studied the combined effects of submergence depth and EMBr on the turbulent flow in both the SEN and in the mold region of a real continuous caster using eight high-resolution LES. Both steady and transient flow fields are presented, and the effects of changes in nozzle flow due to the EMBr are studied. The governing equations, details of the numerical model are given in Section II. Section III describes typical results. Then, the validation of the model is presented in Section IV. Section V and VI discuss the effect of casting speed and effect of SEN submergence depth, respectively. Section VII discusses the effect of EMBr on flow inside SEN, swirls inside the ports and flow in the mold region. Finally, the results are summarized in Section VIII.

## II. GOVERNING EQUATIONS AND COMPUTATIONAL MODEL

### A. Governing Equations for the Fluid Flow

In this work, the turbulent flow in the mold is simulated by the technique of LES. The three-dimensional time-dependent Navier–Stokes equations given below were solved:

$$\nabla \cdot (\rho \mathbf{u}) = \dot{s} \quad [1]$$

$$\begin{aligned} \frac{\partial \mathbf{u}}{\partial t} + \mathbf{u} \cdot (\nabla \mathbf{u}) = & -\frac{\nabla p}{\rho} + \nabla \cdot \left[ (\nu + \nu_{\text{sgs}}) (\nabla \mathbf{u} + (\nabla \mathbf{u})^T) \right] \\ & + \frac{\mathbf{F}_L}{\rho} + \mathbf{S}_{\text{sink}} \end{aligned} \quad [2]$$

where  $\rho$  is the density of molten steel;  $\dot{s}$  and  $\mathbf{S}_{\text{sink}}$  are the mass and momentum sink terms<sup>[25–27]</sup> added to include the effect of the solidifying shell;  $\mathbf{u}$  is the velocity vector,  $p$  is a modified static pressure which includes the normal stresses;  $\nu$  is the kinematic viscosity of the molten steel; and  $\nu_{\text{sgs}}$  is the eddy viscosity that represents the subgrid stress. In this study,  $\nu_{\text{sgs}}$  is modeled by the coherent-structure Smagorinsky model (CSM) subgrid scale (SGS) model.<sup>[28]</sup> This model has been successfully tested and used previously in predicting fluid flow in steel casters with magnetic fields.<sup>[11,16]</sup> A brief introduction of the CSM model is provided in Section II–B, and more details are available elsewhere.<sup>[28]</sup> The term  $\dot{s}$  in the continuity equation is a sink term due to the solidifying shell, and the details about its implementation and the shell profile are given in Section II–C. The imposed magnetic field affects the fluid flow through a Lorentz force field source term  $\mathbf{F}_L$  in the momentum equation. The governing equations for computing  $\mathbf{F}_L$  are discussed in Section II–D. Section II–E discusses the numerical method and the performance of the multi-GPU code. Section II–F presents the geometry of the caster, the computational domain, mesh, boundary conditions, and the computational details.

### B. The CSM Subgrid Scale Model

In LES, the eddy viscosity  $\nu_{\text{sgs}}$  is used to model the influence of the turbulent scales that are not resolved explicitly. In this work, the  $\nu_{\text{sgs}}$  is calculated using a coherent-structure function given by the CSM SGS model.<sup>[28]</sup> The CSM model does not need a wall-damping function. In CSM, first the Smagorinsky eddy-viscosity model is used to compute  $\nu_{\text{sgs}}$  as

$$\nu_{\text{sgs}} = (C_s \Delta)^2 \sqrt{2\|\mathbf{S}\|^2} \quad [3]$$

where  $C_s$  is the Smagorinsky constant;  $\Delta$  is the cell size; and  $\mathbf{S}$  is the rate-of-strain tensor given by  $\mathbf{S} = \frac{1}{2}(\nabla \mathbf{u} + \nabla \mathbf{u}^T)$ . In the CSM model,  $C_s^2$  is calculated locally by the following Eqs. [4] and [5]:

$$C_s^2 = C_{\text{CSM}} \left| \frac{Q}{E} \right|^{3/2} \left( 1 - \frac{Q}{E} \right) \quad [4]$$

$$Q = \frac{1}{2} (\|\mathbf{W}\|^2 - \|\mathbf{S}\|^2) E = \frac{1}{2} (\|\mathbf{W}\|^2 + \|\mathbf{S}\|^2) \quad [5]$$

where  $C_{\text{CSM}} = 1/22$  is a model constant and  $\mathbf{W} = \frac{1}{2}(\nabla \mathbf{u} - \nabla \mathbf{u}^T)$  is the vorticity tensor (also known as rate of rotation tensor). The CSM model appropriately damps the eddy viscosity in wall boundary layer regions and also automatically incorporates the effect of anisotropy induced by the applied magnetic fields on the subgrid scales.<sup>[29]</sup> Therefore, no additional modifications to account for anisotropic subgrid effects are needed or added.

### C. Modeling of the Solidifying Shell

During the casting process, liquid steel continuously solidifies as it crosses the liquid / solid interface which defines the shell. The shell thickness grows as the metal moves downwards in the caster causing the cross section of the liquid metal region to shrink, and the liquid steel mass flow rate to decrease as the phase change progresses from liquid to solid. This reduction in volume of the molten steel is included in our model by imposing the shell profile as the domain boundary and applying a mass sink term in the finite volume cells adjacent to the shell boundary.

The growth of the shell thickness depends on the rate of heat extraction into the mold walls. In this work, a precalculated steady shell profile is applied. The assumed shell thickness  $s$  (mm) at any point  $z$  m below the meniscus is plotted in Figure 1 and it is calculated as

$$s = k \sqrt{z/V_c} \quad [6]$$

where  $V_c$  denotes the casting speed (m/s) and the constant  $k = 3 \text{ mm/s}^{1/2}$  is chosen to match a break-out shell profile from the caster at Baosteel.

A stair-step representation of the shell is used for computational efficiency, considering that the mesh is very refined. Mass and momentum sink terms are added to the cells near the shell to include the effects of the loss in mass due to the solidification. These sink terms are added only in those molten steel cells whose bottom neighbor cell is in the domain of solid shell region as shown in Figure 2. The amount of the mass that leaves the specific cells per second due to solidification is  $\rho V_c \Delta x \Delta y$ , where  $\Delta x$  and  $\Delta y$  are the cell dimensions in the  $x$  (mold width direction) and  $y$  (mold thickness direction) directions, respectively. The momentum associated with this lost mass is subtracted as a momentum sink  $\dot{s} = \rho V_c \Delta x \Delta y / V_{\text{cell}}$ .<sup>[25]</sup>

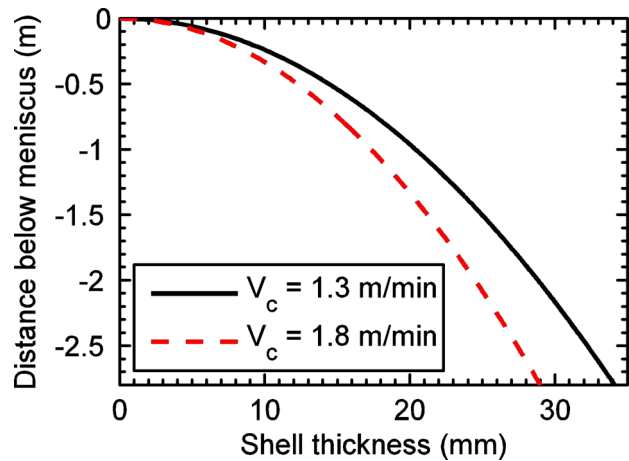


Fig. 1—Shell thickness profile at two casting speeds used in the computational model.

#### D. Equations for MHD Fields and Forces

In this work, an electric potential method is used to compute the Lorentz force. This method exploits the fact that the induced magnetic field is much smaller than the externally imposed magnetic field and therefore can be ignored.<sup>[4,5,8–14,16,24]</sup> When a magnetic field  $\mathbf{B}$  is applied onto a moving conducting material (with electrical conductivity  $\sigma$ ), an electric field is created and the current density  $\mathbf{J}$  can be computed through the Ohm's law given by Eq. [7]. The current conservation law is given by Eq. [8]. The electric potential  $\Phi$  satisfies equation, a Poisson-type equation, (Eq. [9]) from which  $\Phi$  can be solved. The Lorentz force is given by Eq. [10].

$$\mathbf{J} = \sigma(-\nabla\Phi + \mathbf{u} \times \mathbf{B}) \quad [7]$$

$$\nabla \cdot \mathbf{J} = 0 \quad [8]$$

$$\nabla \cdot (\sigma \nabla \Phi) = \nabla \cdot [\sigma(\mathbf{u} \times \mathbf{B})] \quad [9]$$

$$\mathbf{F}_L = \mathbf{J} \times \mathbf{B} \quad [10]$$

Note that both the molten steel and the solidified shell are conducting materials, so Eqs. [7] through [10] must be solved in both the liquid steel and shell regions. Replacing the shell with an electrically insulated wall boundary condition leads to incorrect results.<sup>[11,12]</sup>

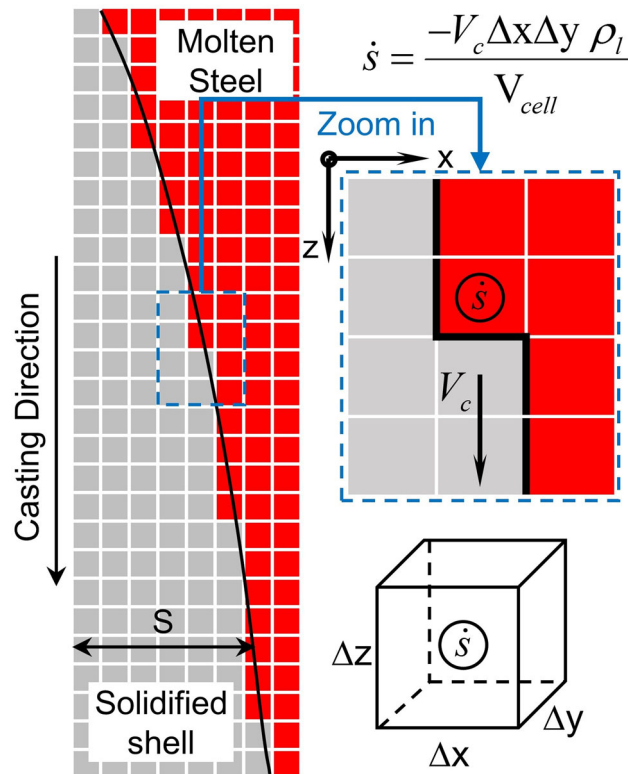


Fig. 2—Schematic of grid near solid shell showing a cell with non-zero mass sink terms.

Thus, in this work, the above MHD equations are solved in the entire domain including the solid shell region. An insulated wall is applied at the exterior of the shell, considering that the slag in the mold/shell gap has very low conductivity.

#### E. Numerical Method and Code Validation

Previous LES simulations of steel caster flow fields have been limited by computational resources, so only relatively coarse grids were used and parametric studies were not feasible. In the present work, to accelerate computation speed, the governing equations are solved on multiple graphics processing units (GPU). An in-house code CUFlow,<sup>[30–34]</sup> written in CUDA Fortran language, has been extended to multiple GPUs in parallel through the message passing interface.<sup>[33]</sup> This multi-GPU code has high parallel efficiency and exploits larger GPU memory. CUFlow has been validated in studies of magnetohydrodynamic flow in a square lid-driven cavity,<sup>[35]</sup> generalized Newtonian fluid flow,<sup>[36]</sup> bubble rise in duct,<sup>[37,38]</sup> and flow in the mold region of continuous casters of steel with and without EMBr.<sup>[11,12,16]</sup>

The calculations in this paper were performed on the GPUs of Blue Waters supercomputer at the National Center for Supercomputing Applications, Illinois. The computational domain was decomposed in the casting direction and uniformly distributed onto six NVIDIA Kepler K20x GPUs. A fractional step method is used to solve the continuity and momentum equations. Complete details of the solution algorithm are given elsewhere.<sup>[31–33]</sup> The most computationally intensive parts are the solution of the two Poisson equations (pressure-Poisson equation and electrical-Poisson equation). In this work, the two Poisson equations are solved efficiently on GPUs by a V-cycle multigrid method, and red-black successive overrelaxation with overrelaxation parameter of 1.6.

#### F. Computational Domain, Mesh, Boundary Conditions, and Computational Cost

This work studies flow in the No. 4 steel caster in Baosteel, Shanghai, P. R. China. The casting parameters, flow domain, and steel properties are given in Table 1.

A 3D view of the liquid steel region of the computational domain is shown in Figure 3. A Cartesian grid with approximately 16 million finite volume cells (cell size ~4 mm) was used to discretize the computational domain which included the slide gate, SEN, and mold region of the caster. The domain extends to 2.6 m below the meniscus. To incorporate the effect of the solidified shell on the electrical current and Lorentz force distributions, the solid shell is included in the computational domain by adding solid cells on the sides of the liquid region. In these cells, the fluid flow equations are not solved, but only the MHD equations are solved. For these cells, the velocity component in the casting direction ( $z$  direction) is prescribed to be the casting speed, with other velocity components being zero. The



**Table I. Casting Parameters and Steel Properties**

Process parameters	Value
Mold thickness ( $L_t$ , mm)	230
Mold width ( $L_w$ , mm)	1200*; 1300
Slide gate opening area fraction	70 pct*; 80 pct
Submergence depth ( $d_{sub}$ , mm)	170*; 200
SEN port downward angle	15°
SEN port area (width × height, mm × mm)	65 × 83
Casting speed ( $V_c$ , m/min)	1.3*; 1.8
Steel density ( $\rho$ , kg/m <sup>3</sup> )	7000
Steel dynamic viscosity ( $\mu$ , kg/(m s))	0.0063
Liquid steel electrical conductivity ( $\sigma$ , S/m)	714000
Solid steel electrical conductivity ( $\sigma$ , S/m)	787000

\* Casting conditions of the plant measurements.

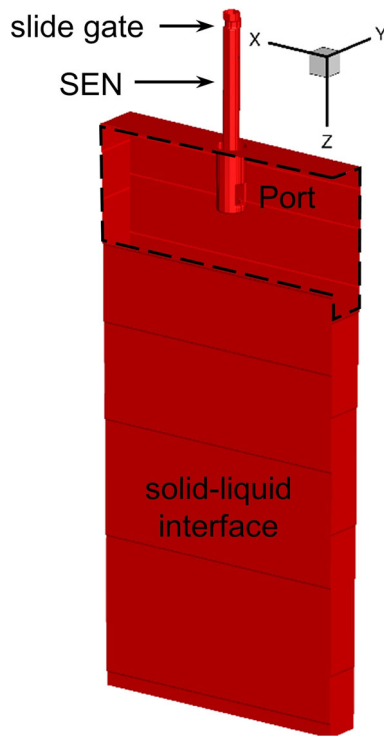


Fig. 3—Computational domain (cells in the solid shell region are hidden).

rate of flow of the molten steel through the SEN into the mold is controlled by the slide gate that moves between the geometric center and the inside radius of the caster, as indicated in Figure 4. To get a casting speed of 1.8 m/min, the slide gate was kept 80 pct open and the molten steel flow first entered the inner radius region of the SEN.

The fluid velocity at the SEN inlet is fixed at 1.66 m/s to match total the mass flow rate of the steel. At the outlet, zero derivative boundary conditions are applied. All other domain boundaries and the interface between the liquid steel and solidified shell are prescribed as no slip and no penetration conditions. As mentioned earlier, the MHD equations, an insulated boundary condition is applied at the outer most boundary of the

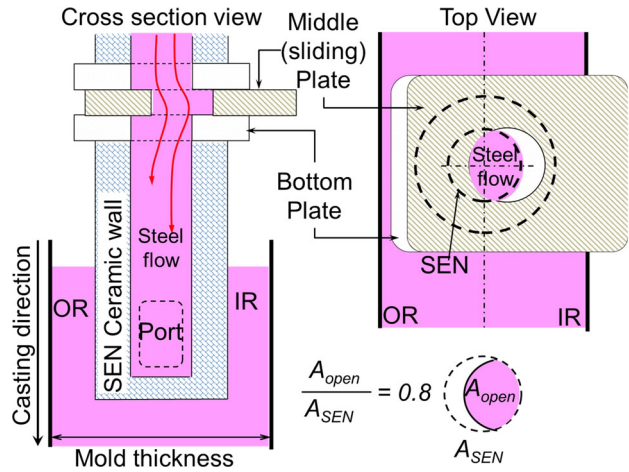


Fig. 4—Slide gate showing asymmetric flow in upper nozzle, 80 pct open with casting speed of 1.8 m/min.

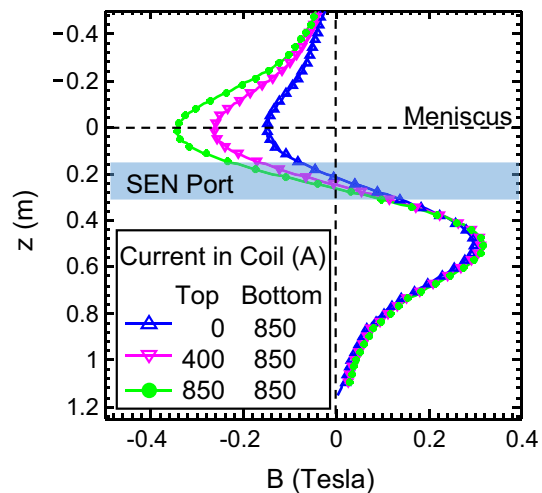


Fig. 5—Measured magnetic field showing measurement points (dots) and interpolated (lines) used in model. Adapted from Jin *et al.*<sup>[39]</sup>

computational domain and the shell is considered electrically conducting.

This work investigates turbulent flow with the double-ruler EMBR system. The induced magnetic fields for three different configurations of the coil current were measured at Baosteel.<sup>[39]</sup> Figure 5 shows the magnetic field strengths measured at discrete points and the interpolated magnetic field that is used in the calculations. The top surface (molten-steel/slag layer interface) is at  $z = 0$ , and the location of the submerged nozzle ports is shown as a shaded region. All three current levels of the upper ruler have very weak magnetic field strength across the ports, similar increasing strengths below the ports, and increasing strengths above the ports, reaching different peaks, depending on the coil current. With the coil current of 400 and 850 A, the maximum magnetic field strength near the meniscus is  $1.8\times$  and  $2.5\times$  larger than that with zero top coil current. Note that with a double-ruler system, even

when the top coil has zero current, there is still a local peak magnetic field ( $-0.14$  T) generated near the top electromagnet. Thus, the field profile is different from that of a single ruler system, positioned at the lower electromagnet location. The measurements show that the variations of the magnetic field along the mold thickness and width are very small in all three cases, so the imposed magnetic field only varies in the casting direction ( $z$  direction).

As listed in Table II, eight LES simulations were carried out on the Blue Waters supercomputer. All simulations were started with zero initial velocity, and the flow fields were allowed to develop for 15 seconds of real flow time. After that, turbulence statistics were collected for  $\sim 25$  seconds until the simulation finished at  $\sim 40$  seconds. Specifically, velocity and pressure were stored in selected slices (Figure 6). The selected slices included the symmetry center planes ( $x = 0$ ;  $y = 0$  m), the port exit planes ( $x = \pm 0.047$  m), and a parallel plane 1 cm below the top surface ( $z = 0.01$  m). A time step around  $0.0002$  second was used for stability. At each time step, convergence was defined when the pressure residual reduced by four orders of magnitude, reaching  $\sim 1 \times 10^{-8}$ . Typically on six GPUs about two days (144 node hours) were required to complete a 40 seconds LES simulation on a grid with  $\sim 16$  million cells.

### III. TYPICAL RESULTS

The first simulation was performed at low casting speed, without EMBr, for conditions where measurements were available for model validation. Specifically, 80 seconds were simulated on a grid of 15.5 million cells for the conditions given in Table I.

#### A. Flow in the SEN and Port

Figure 7(a) shows contours of the time-averaged vertical velocity  $\bar{u}_z$  in the symmetry plane of the SEN. The high-velocity jet flowing the slide gate opening first enters the inner radius side of the SEN with a maximum velocity slightly above  $2$  m/s. The jet is then deflected off of the SEN side wall and flows stronger down the outer radius wall side, forming a strong counter-clockwise swirling flow at the bottom of the SEN. Close to the

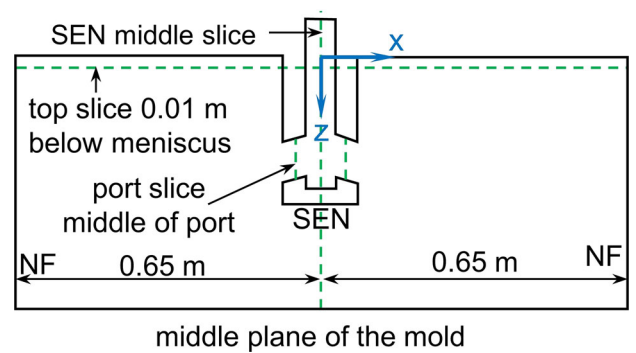


Fig. 6—Location of important surfaces.

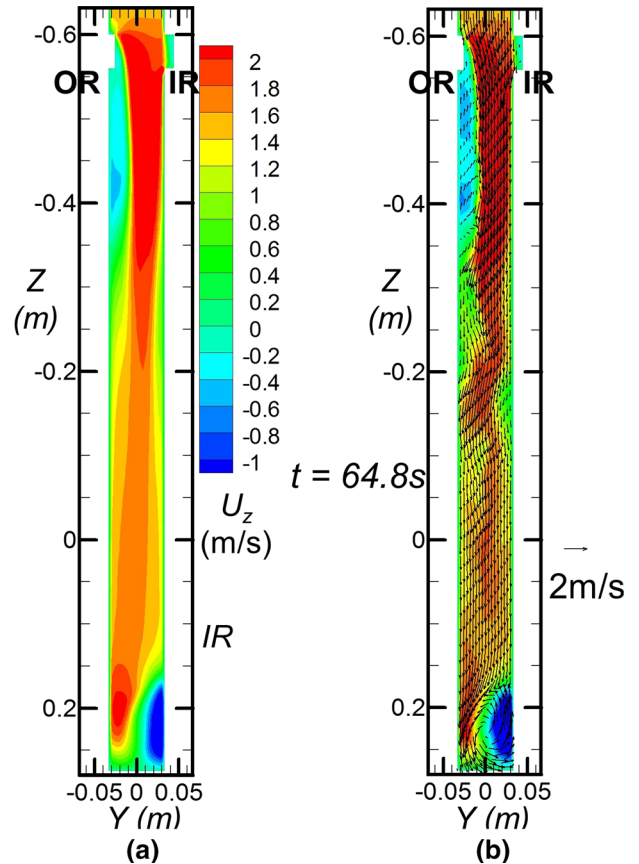


Fig. 7—(a) Contours of time-averaged  $u_z$  velocity in centerplane of SEN; (b) snapshot of transient  $u_z$  at  $t = 64.8$  s.

Table II. List of the Eight LES Simulations

Submergence Depth (mm)	Top Coil Current (A)	Bottom Coil Current (A)	Casting Speed (m/min)	Mold Width $\times$ Thickness (m $\times$ m)
170*	0	0	1.3	$1.2 \times 0.23$
170	0	0		
	400	850		
	850	850		
200	0	0	1.8	$1.3 \times 0.23$
	0	850		
	400	850		

\* Conditions of the plant measurements.<sup>[39]</sup>

slide gate, a 0.3-m long recirculation zone starting inside the sliding plate forms and occupies almost half of the SEN diameter. This large recirculation region and the bottom swirl are also seen in Figure 7(b) which shows an instantaneous vertical velocity field at  $t = 64.8$  seconds. However, this snapshot shows that the jet bounces several times before it reaches the bottom of the SEN.

Figure 8(a) shows contours of the time-averaged  $x$  velocity ( $\bar{u}_x$ ) at the port exit plane (see location in Figure 6). The large counter-clockwise swirl structure observed in the SEN bottom (Figure 7) extends through the port. In Figure 8, negative  $\bar{u}_x$  means flow is leaving the SEN and entering the mold, while a positive  $\bar{u}_x$  indicates flow reversal going back into the port from the mold as a “back-flow” region. On average, the flow leaves the SEN closer to the outer radius side of the port, with an average velocity of 1 m/s. Two back-flow regions are found inside the port: one near the middle (biased toward the inner radius side) and the other at the top and outer radius side of port. The back-flow can make the jet unstable and substantially alter the mold flow pattern.<sup>[40,41]</sup> These back-flow regions together occupy about one quarter of the entire port area. The middle back-flow region is formed due to the strong swirl structure, which generates a local low-pressure region that sucks fluid into the center of the swirl. A snapshot of flow in the port shown in Figure 8(b) indicates that the maximum velocity leaving into the mold is around 1.5 m/s and the back-flow is as large as 1 m/s.

A snapshot of the isosurface of constant  $u_x$  velocity is shown in Figure 9 and illustrates the complex 3D structure of the jet that enters the mold region. The jet enters the mold with a higher velocity near the top outer radius corner of port. At that corner, and in the middle of the port, the back-flow regions are seen (with yellow color). The structure of the jet leaving the port is caused by the swirl residing at the bottom of the SEN, which has its root cause in the slide gate position and the casting speed.

## B. Flow in the Mold Region

The flow in the middle plane of the mold and top surface is shown in Figure 10. Close to the SEN, the mean flow speed is smaller than 0.1 m/s. The jet has higher speed near top and bottom of the ports, (sometimes called the “nose structure” and main lower jet). This is due to its 3D swirling shape, as shown in Figure 9. It is necessary to note that the instantaneous flow speed close to the SEN often changes directions and is usually much higher than the mean value. The low average speed shown is mainly caused by cancellation of the different instantaneous flow directions.

Figure 10(a) shows at one centimeter below top surface that the flow direction is mainly from NF to SEN in most regions, and the maximum mean velocity magnitude is about 0.2 m/s near the quarter mold width. At regions very close to the NF, the flow direction is toward NF, which is caused by a small, weak secondary circulation region at the corner of the mold, that is less than 0.1 m/s. Figure 10(b) shows the flow streamlines in

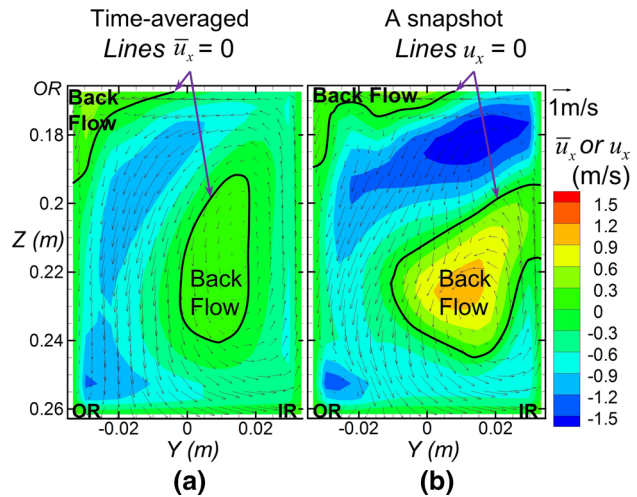


Fig. 8—(a) Time-averaged  $x$  velocity.  $\bar{u}_x < 0$ , flow enter mold;  $\bar{u}_x > 0$ , back flow—reversal going into port (b) a snapshot of  $u_x$  at  $t = 64.8$  s.

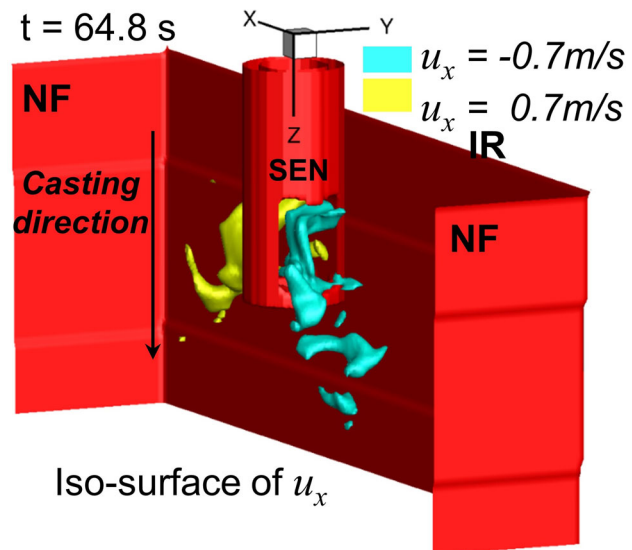


Fig. 9—Steel shell, SEN, and isosurface of constant  $u_x = \pm 0.7$  m/s at  $t = 64.8$  s.

the middle plane of the mold. As expected, a classic double-roll flow pattern is seen in the mold region, with large, nearly symmetrical, counter-rotating recirculation regions both above and below each of the jets.

The swirl direction exiting the port is also important and several previous works have discussed the relation of the swirl flow in the SEN with the bulk flow in the mold.<sup>[40,42]</sup> Here, the swirl at the bottom of the SEN has three different patterns as shown in Figure 11: (1) two symmetrical swirls of almost equal size at the bottom of the SEN; (2) one generally clockwise swirl that rotates from inner radius side to outer radius side across the nozzle bottom; (3) one counter-clockwise swirl that rotates from outer radius side to inner radius side. Figure 12 shows the swirl types at different times of the simulation and the corresponding top surface velocity in the mold. For this low casting speed, the predominant



swirl direction is counter-clockwise, generated from stronger flow down the outer radius, crossing the bottom to the inner radius. This is counter intuitive because the steel flow first enters down the inner radius side of SEN. However, the jet enters the SEN from the slide gate at an angle, which causes the core of the jet to bounce off the inner radius toward the outer radius of the SEN inner wall. Thus the swirl direction is not only related to the position of the slide gate (which varies with casting speed), but also depends on the SEN length. The time histories of  $u_x$  velocity component at the center plane, quarter mold region, and 1 cm below top surface are shown in Figure 12. In these histories, no significant

relation is seen between the top surface velocity and the swirl direction. This is likely due to the short periods (<2 seconds) of clockwise swirl, which are much shorter than the recirculation time in the upper roll.

#### IV. MODEL VALIDATION

The simulation presented in the previous section was validated with measurements of surface velocity in the mold. Surface velocity of the molten steel in the mold is critical to the final quality of the product. Various techniques such as nail-board dipping method<sup>[43]</sup> and

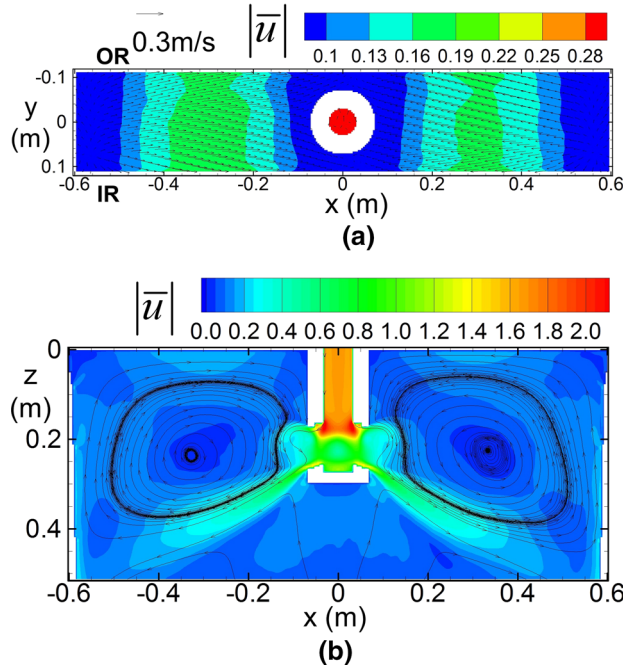


Fig. 10—Contours of time-average velocity magnitude at (a) 1 cm below top surface and (b) in mold centerplane.

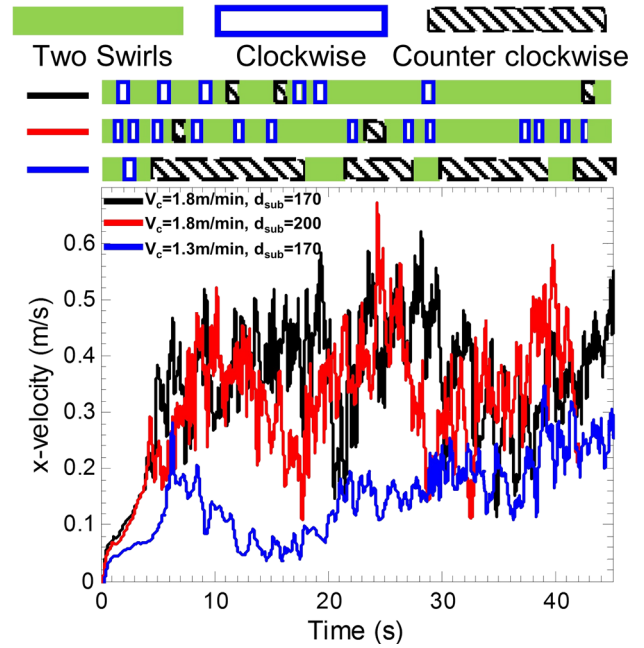


Fig. 12—Surface  $x$  velocity and swirl rotation in port (looking into right port). Black line:  $V_c = 1.8$  m/min and  $d_{sub} = 170$ ; Red line:  $V_c = 1.8$  m/min and  $d_{sub} = 200$  mm; Blue line:  $V_c = 1.3$  m/min and  $d_{sub} = 170$  mm (Color figure online).

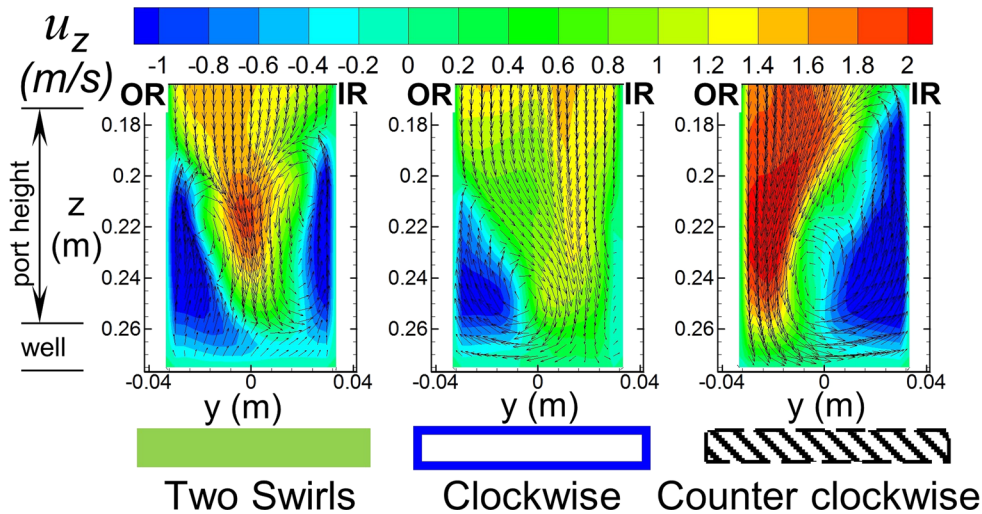


Fig. 11—Swirl at bottom of SEN (low casting speed of 1.3 m/min).



submeniscus velocity control devices<sup>[44]</sup> have been previously used to measure the surface velocity. In this work, a rod-deflection device (similar to a previous inclination method<sup>[45]</sup>) was used to measure the surface velocity.<sup>[39]</sup> The test consists of measuring the deflection angle of a rod (probe) about its pivot point while its other end is dipped into the molten steel. The molten steel flow impinges on the rod and generates a drag force which balances the weight of the rod after it rotates an angle of  $\theta$ . This angle is then converted into a velocity parallel to the wide face (WF) of the mold. These measurements were performed at Baosteel No. 4 caster with a strand size of 230 mm  $\times$  1200 mm, casting speed of 1.3 m/min, and a 70 pct slide gate opening pct. No argon gas was injected, and the EMBr system was turned off during the measurements. The device probe was placed between the SEN and NF (as shown in Figure 13) and the measured steel surface velocity was recorded every 5 seconds during a seventy second interval.

The  $x$  direction velocity (parallel to WF) calculated at the probe location of 1 cm below the top surface and at the quarter mold region in the middle plane is compared with the measurement in Figure 13. Both the LES simulations and the measurements show that the flow direction is from NF to the SEN, with an average velocity around 0.2 m/s. Also, both show that the surface velocity sometimes drops to a relatively low value of 0.12 m/s for 10-20 seconds, and at other times it can be twice as big. The velocity changes with a low frequency of 0.025 to 0.05 Hz. This agreement between the computations and measurements gives confidence in the LES approach.

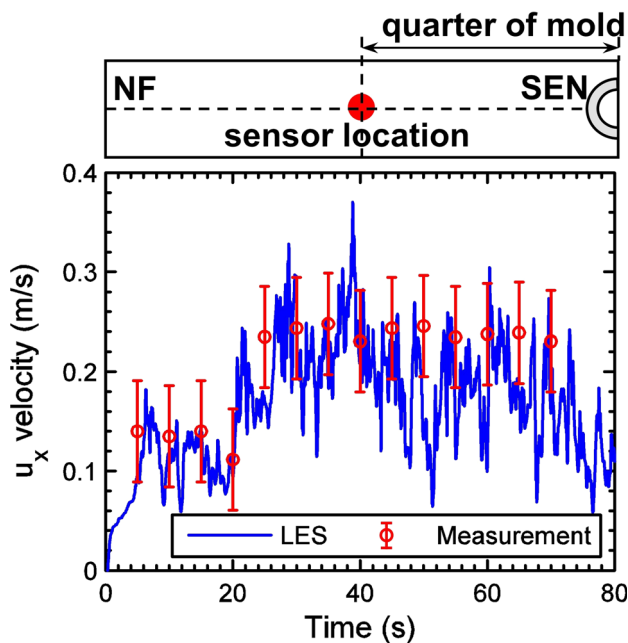


Fig. 13—Comparison of predicted surface velocity (centerplane, quarter mold, 1 cm below top surface) with plant measurements. Adapted from Jin *et al.*<sup>[39]</sup>

## V. EFFECT OF CASTING SPEED

Seven simulations were next conducted at high casting speed of 1.8 m/min to study the effects of submergence depth and EMBr on the flow in the caster, for conditions given in Table II. All figures shown in the rest of this paper are at this higher speed.

### A. Flow in SEN Ports

Figure 14 shows contours of time-averaged  $x$  velocity ( $\bar{u}_x$ ) (in/out of port) in a cross section through the port at  $x = -0.45$  m at the high casting speed. Two symmetrical counter-rotating swirls persist for most of the time. This contrasts with low casting speed, where a single swirl with counter-clockwise rotating flow is seen, in Figure 8. This is likely due to the larger slide gate opening needed to achieve the higher casting speed, which produces less asymmetrical flow down the side of the SEN. The black line is where  $\bar{u}_x = 0$ . Inside and at the upper portion of the port, a back-flow region is seen. This region occupies about 15 pct of the total port cross section area, with an inward velocity  $\bar{u}_x$  less than 0.5 m/s. This is caused by the jet entering the mold region from the lower portion of the SEN port.

Comparing Figure 8(a) with Figure 14, shows that the back-flow region entering the upper port at high casting speed is much larger than that at low casting speed. At low casting speed, a second back-flow region appears at the center of the single, strong, counter-clockwise swirl. A low-pressure region forms in the center low-velocity region of this large swirl, which during some instants can even suck in fluid from the surrounding. High casting speed produces two small, but weak symmetrical swirls, exiting into the mold from near the port bottom. These small swirls are not strong enough to form a low-pressure region or to suck in liquid steel from the mold.

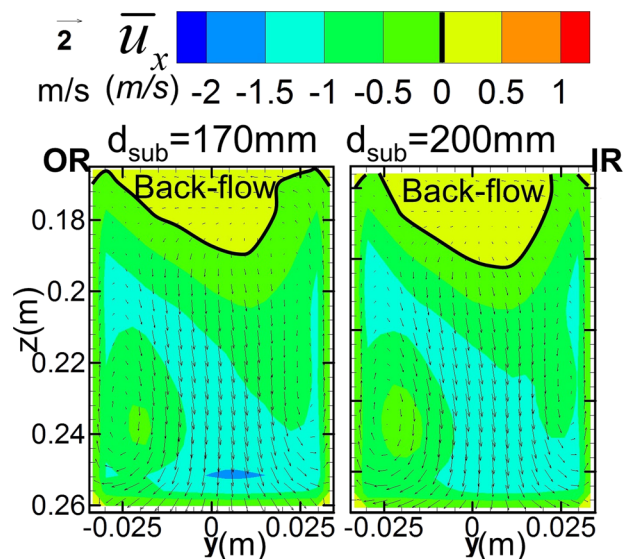


Fig. 14—Effect of submergence depth on time-averaged velocity and swirl in port (1.8 m/min, no EMBr).

## B. Mold Flow

The mold flow at both casting speeds shows a typical double-roll pattern. At low casting speed of 1.3 m/min, a nose structure is seen at near the top port exit, but it disappears at higher casting speed, as the single strong swirl becomes two small weak swirls. At high casting speed, a low-frequency ( $\sim 0.03$  to  $0.04$  Hz) variation of the top surface  $x$  direction velocity is seen for both submergence depths. The top surface velocity at quarter mold region is increased from  $\sim 0.2$  m/s (at  $V_c = 1.3$  m/min) to  $\sim 0.385$  m/s (170 mm submergence) or  $0.325$  m/s (200 mm submergence).

## VI. EFFECT OF SUBMERGENCE DEPTH

Submergence depth changes regularly during the plant operation, in order to lessen the effects of refractory erosion at the interface with the liquid slag and steel top surface.

### A. Mold Flow

Modifying submergence depth changes the flow pattern in the mold and affects the top surface velocity, level fluctuations, and meniscus heat transfer.<sup>[46]</sup> When an EMBR system is used, the submergence depth affects the mold flow as well as the EMBR efficiency.<sup>[18]</sup> Contours of time-averaged velocity magnitude  $|\bar{u}|$  in the middle plane of the mold and 1 cm below top surface are shown in Figure 15 for two different submergence depths with no EMBR. The stream traces in the middle center plane show a typical double-roll flow pattern for both submergence depths.

Increasing the submergence depth by 17 pct is seen to cause a 15 pct decrease in top surface mean flow velocity, although the surface level fluctuations are less affected. This agrees with conventional expectations, but it should be emphasized that this trend is not general and depends on the specific casting conditions.

Because of the high resolution in the LES approach, smaller recirculation zones at the corner between NF and top surface were resolved. Each small recirculation zone spans  $\sim 70$  mm and rotates with a smaller downward velocity (0.05 to 0.1 m/s) at the side close to the NF. This downward velocity may increase the chance of slag entrainment and capture of the inclusion particles as well as argon bubbles.<sup>[47,48]</sup>

### B. Surface Flow

Near the top surface, the fluid moves almost parallel to the wide face at a speed of  $\sim 0.35$  m/s without any cross flow. This is slightly higher than suggested optimal surface velocity ranges: higher than 0.1 to 0.2 m/s<sup>[49]</sup> and less than 0.3 m/s<sup>[50]</sup>  $\sim 0.4$  m/s.<sup>[49]</sup> A lower surface velocity causes inadequate heat transfer to melt the slag powder and leads to entrapment of slag particles and freezing of the meniscus. A higher velocity on the other hand may cause shear instabilities and level fluctuations which can entrain slag and cause other surface defects.<sup>[39,49,51]</sup> The contour lines with a velocity magnitude of  $|\bar{u}| = 0.4$  m/s and  $|\bar{u}| = 0.1$  m/s are marked with thicker black and red lines, respectively. Higher velocity regions are found close to the outer radius side of the wide face. This biased flow velocity shows that although the slide gate asymmetry may not lead to a cross flow near the meniscus region, it may cause stronger flow at the outer radius side. However, the time-averaged values can be

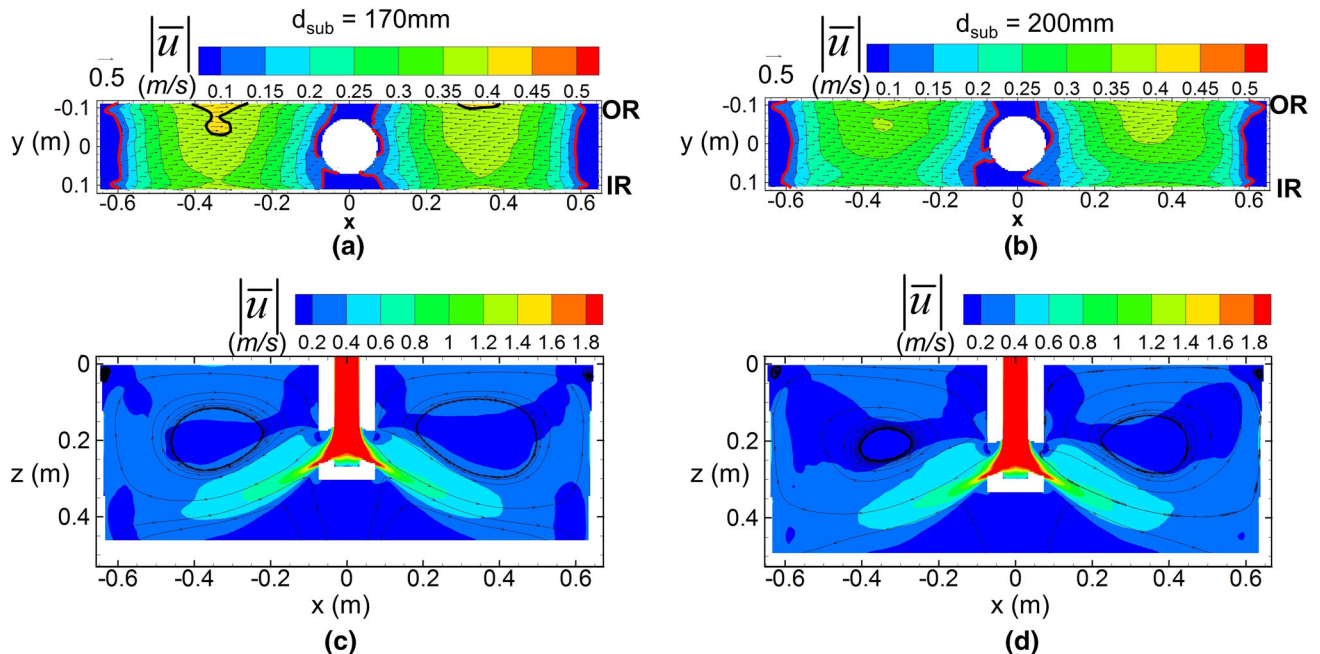


Fig. 15—Effect of submergence depth on velocity in mold. (a) and (b) show flow at 1 cm below top surface; (c) and (d) show flow in mold centerplane. (Vectors shown at only 1/30 of all grid points.) Adapted from Jin *et al.*<sup>[39]</sup>

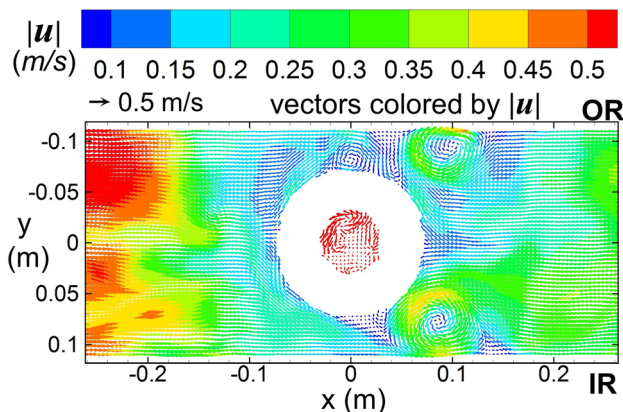


Fig. 16—Snapshot of instantaneous velocity at top surface (no EMBR).

misleading because they do not show regions of large flow fluctuations, where changing flow directions cancel their effect during computing the mean velocity. A snapshot of the flow close to the SEN is shown in Figure 16, which shows locations near the SEN with local velocity magnitude higher than 0.4 m/s. These high-velocity vortices can result in slag entrainment into the molten steel and defects in the final product if captured by the shell.<sup>[43]</sup>

## VII. EFFECT OF EMBR

### A. Flow in SEN

Previously,<sup>[16,17]</sup> the double-ruler EMBR has been shown to be able to stabilize the flow in the mold region and to reduce surface fluctuations. However, previous studies have not noted the effect of EMBR on turbulent flow inside the nozzle, and its effect on the swirling flow exiting the ports. Many previous numerical models did not include the geometry of the full SEN<sup>[7–15,22,24]</sup> or simply applied a zero magnetic field inside the SEN.<sup>[16]</sup> However, plant measurements indicate that the magnetic field generated by the top ruler is strong inside the SEN, and only decays to zero close to the slide gate. Therefore, a strong transverse magnetic field typically exists through a large portion of the nozzle, and influence nozzle flow and jet behavior. Figure 17 shows the time-averaged  $z$  velocity  $\bar{u}_z$  in the symmetry plane ( $x = 0$ ) of the SEN with casting speed of 1.8 m/s. It is seen that the flow separates when it exits the middle sliding gate and reattaches about 0.2 m below the separation point. A recirculation region of 0.2 m long and almost half the SEN diameter forms. This large recirculation region can cause clogging as well as aspirating in gas due to its low pressure. Because of the weak magnetic field near the slide gate region, reattachment is not significantly altered, but the velocity inside the recirculation zone is slightly reduced. As magnetic field strength increases down the SEN, the flow is reattached and the jet slows down. The jet penetration length, defined as the distance from the slide

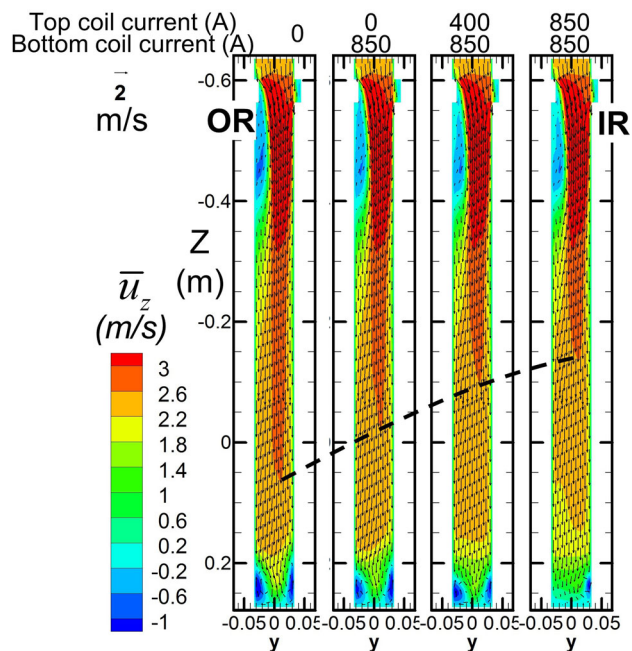


Fig. 17—Time-averaged flow in SEN symmetry plane ( $x = 0$ ) under different magnetic fields. Contour of  $\bar{u}_z$ . Adapted from Jin *et al.*<sup>[39]</sup>

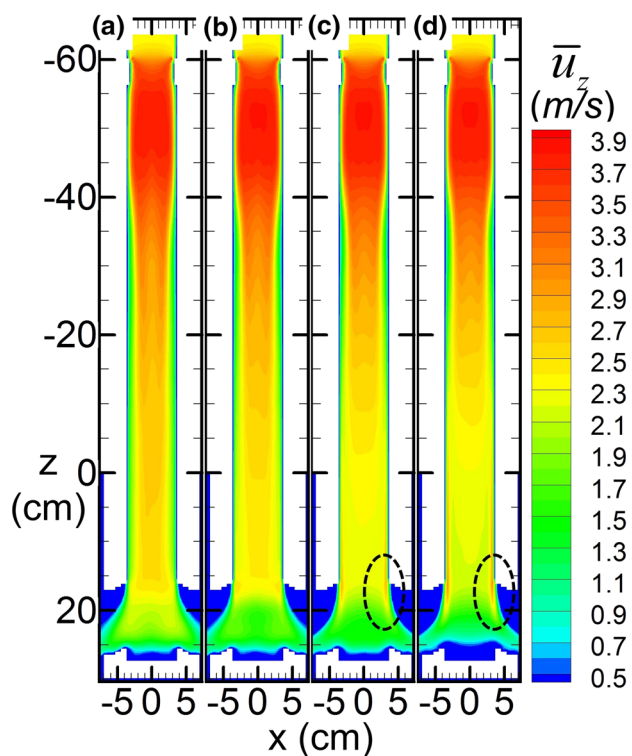


Fig. 18—Contour of  $\bar{u}_z$  in SEN centerplane. (a) No EMBR; (b) bottom coil current 850 A; (c) top coil current 400 A and bottom coil current 850 A; (d) both coils have current of 850 A.

gate to where the maximum jet velocity drops to 2.6 m/s, becomes smaller. Two counter-rotating swirls are usually seen at the bottom of the SEN. When the top coil current increases to 850 A; however, only one tiny



swirl region is observed at the inner radius side of the nozzle.

Figure 18 shows the time-averaged  $\bar{u}_z$  velocity in the middle plane ( $y = 0$ ) of the SEN for different magnetic field strengths. It can be seen that close to the slide gate, the maximum velocity can be as large as 4 m/s. With a strong magnetic field, higher velocity layers are seen close to the SEN wall in the lower part of the SEN. The jets leaving the SEN ports also become thinner with increasing strength of the applied magnetic field.

To reveal the thin high-velocity regions in the lower SEN caused by EMBr, Figure 19 plots the time-averaged  $\bar{u}_z$  velocity across the SEN at 0.15 m below the liquid level in the mold. An “M-shaped” velocity profile is seen with EMBr, with the velocity peak increasing with field strength. The maximum streamwise velocity in the M-shaped profile is around 2.8 m/s for the strongest magnetic field of the top coil, with current of 850 A.

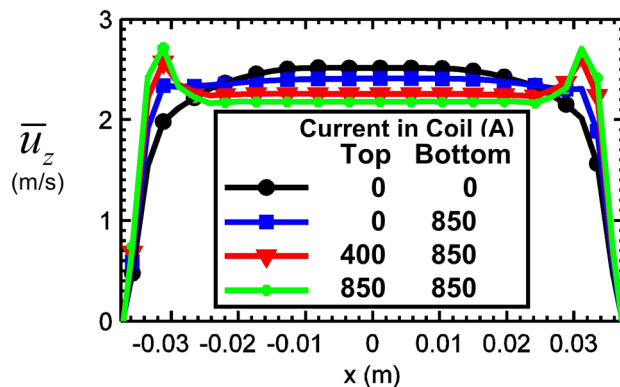


Fig. 19—Time-averaged profile of  $\bar{u}_z$  in SEN at  $z = 1.5$  m and  $y = 0$ .

This M-shaped profile is commonly seen in channel and duct flows<sup>[52,53]</sup> when a strong transverse magnetic field is applied. However, to our knowledge, this is the first study to report an M-shaped profile in the SEN of a continuous caster. As the magnetic field strength increases, the M-shaped profile becomes steeper and

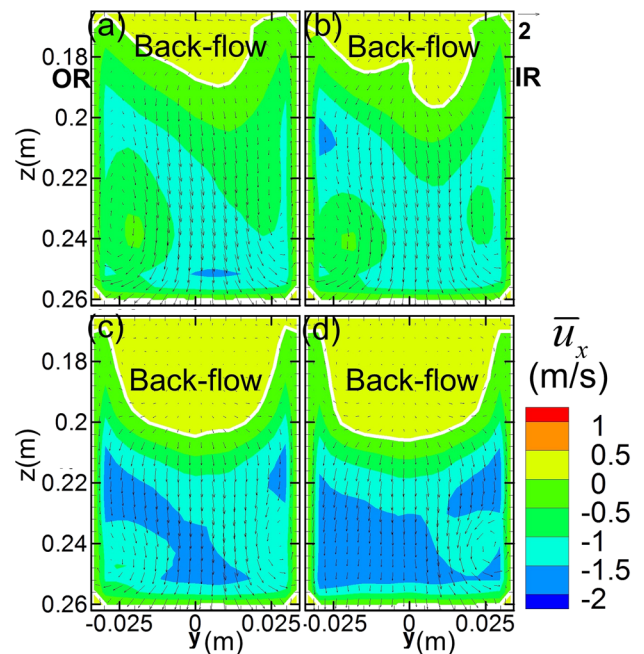


Fig. 21—Contours of time-averaged  $x$  velocity in port (positive  $x$  velocity means back-flow) for  $d_{\text{sub}} = 170$  mm with different EMBr: (a) without EMBr (b) bottom coil current 850 A; (c) top coil 400 A and bottom coil 850 A; (d) both coils 850 A. Adapted from Jin *et al.*<sup>[39]</sup>

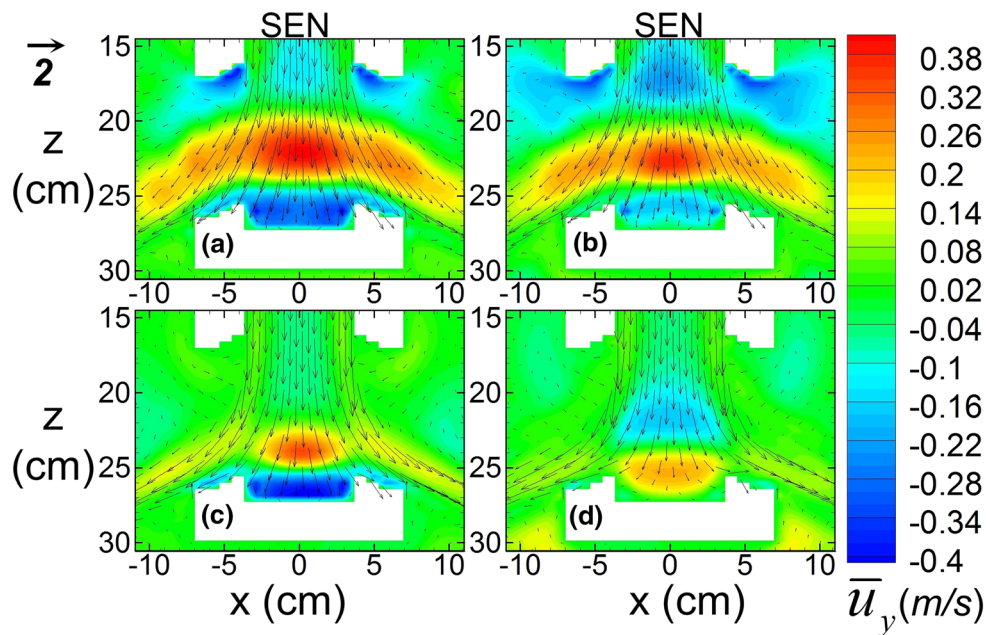


Fig. 20—Velocity at bottom of the SEN. Positive  $y$  velocity means flow exiting port (a) No EMBr; (b) bottom coil current 850 A; (c) top coil current 400 A and bottom coil current 850 A; (d) both coils have current of 850 A.



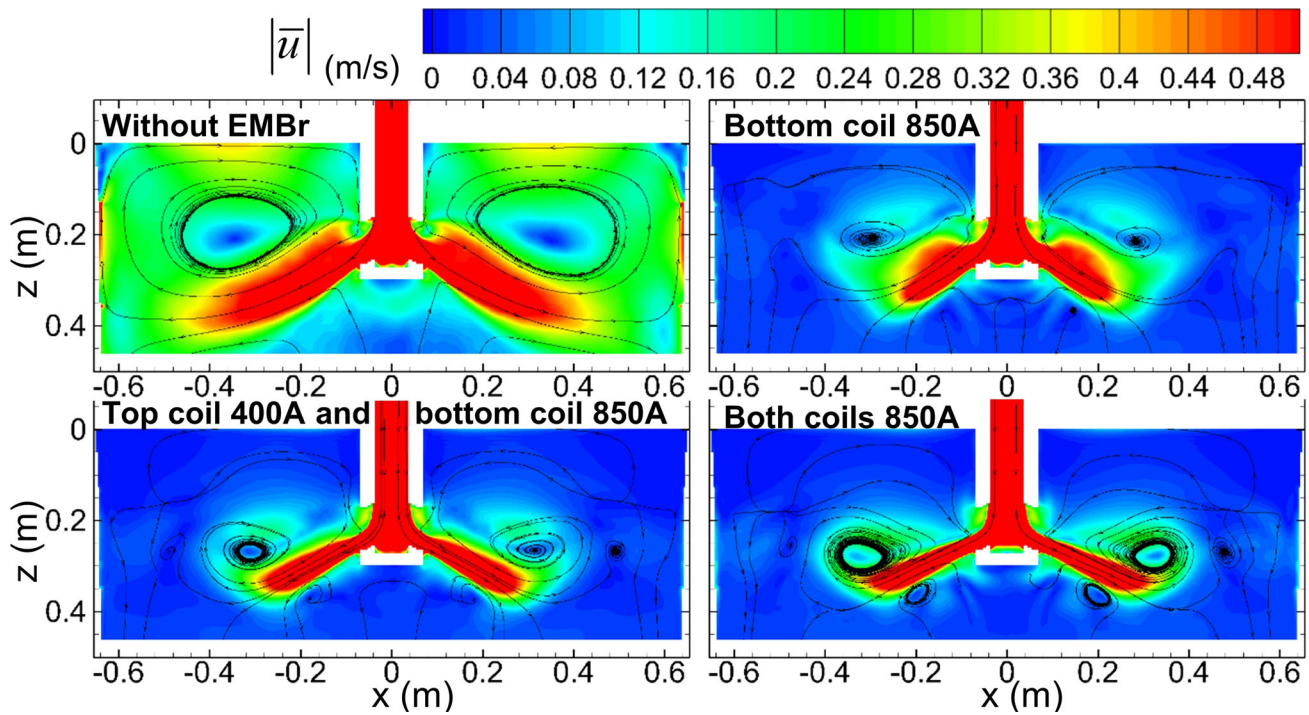


Fig. 22—Time-averaged velocity magnitude  $|\bar{u}|$  in middle plane of the mold.

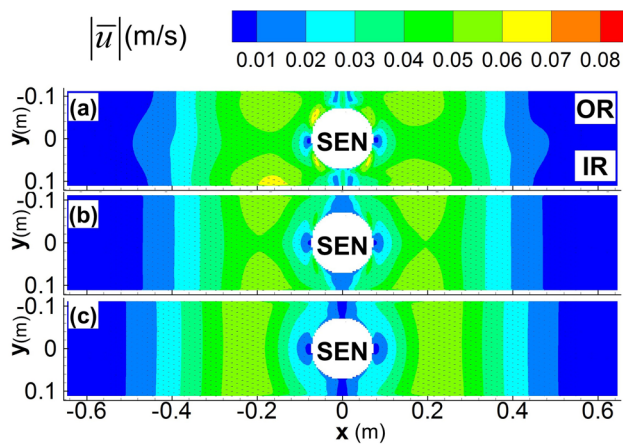


Fig. 23—Contours of time-averaged velocity magnitude at 1 cm below top surface (a) bottom coil current 850 A; (b) top coil current 400 A and bottom coil current 850 A; (c) both coils have current of 850 A.

forms at higher locations inside the SEN. This M-shaped profile has higher momentum near the SEN side walls. As the jets exit the SEN, the high-velocity layer is bent by the bottom angle of the port. However, its high momentum causes the jet to penetrate the mold region as a thinner and stronger jet leaving the bottom of the port. To satisfy local mass conservation, a larger back-flow region inside the upper port is expected. These findings show that it is important to including the magnetic field inside the SEN when studying flow in the mold with EMBR.

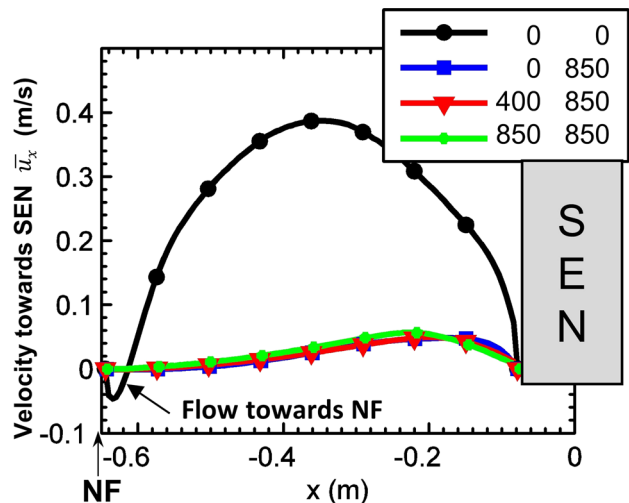


Fig. 24—Mean  $x$  velocity across center line 1 cm below top surface. (Legend shows current (A) in top and bottom coils).

## B. Swirl Flow in the Ports

A strong swirling flow extends across the SEN bottom and through both ports, which is caused by the asymmetric flow down the nozzle. In Figure 20, time-averaged  $y$  direction velocity ( $\bar{u}_y$ ) contours are shown, which reveal this swirling region. Increasing the magnetic field strength reduces the size and strength of this swirl. With a magnetic field, the swirl is confined to only a small region near the central axis, and flow exiting the ports has no swirl.

Figure 21 shows the effect of magnetic field strength on the time-average flow at port exit. The sizes of the

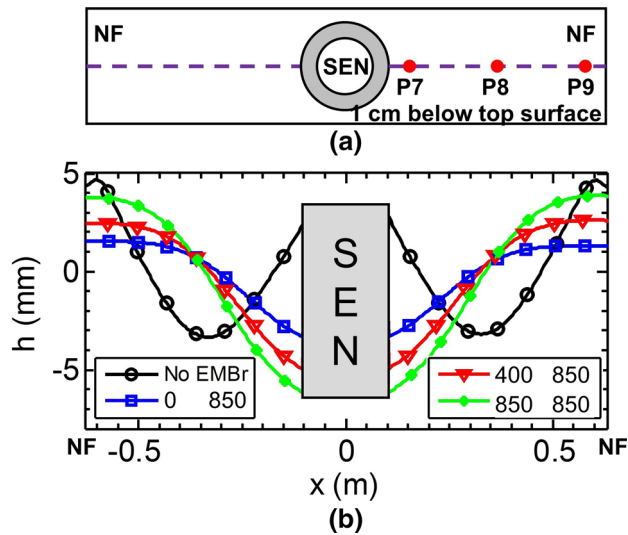


Fig. 25—(a) Top view showing points where pressure data were obtained on centerplane. (b) Predicted surface level profiles for cases with submergence depth 170 mm. (Legend shows current (A) in top and bottom coils).

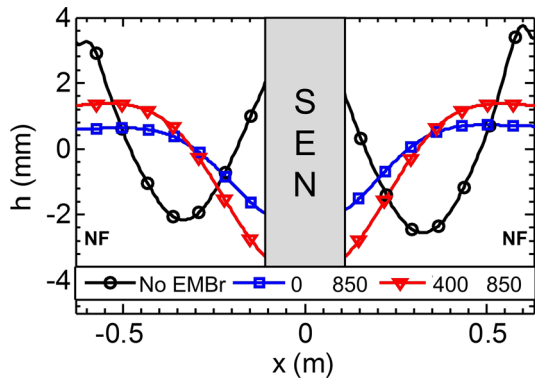


Fig. 26—Predicted surface level profile for cases with submergence depth 200 mm. (Legend shows current (A) in top and bottom coils).

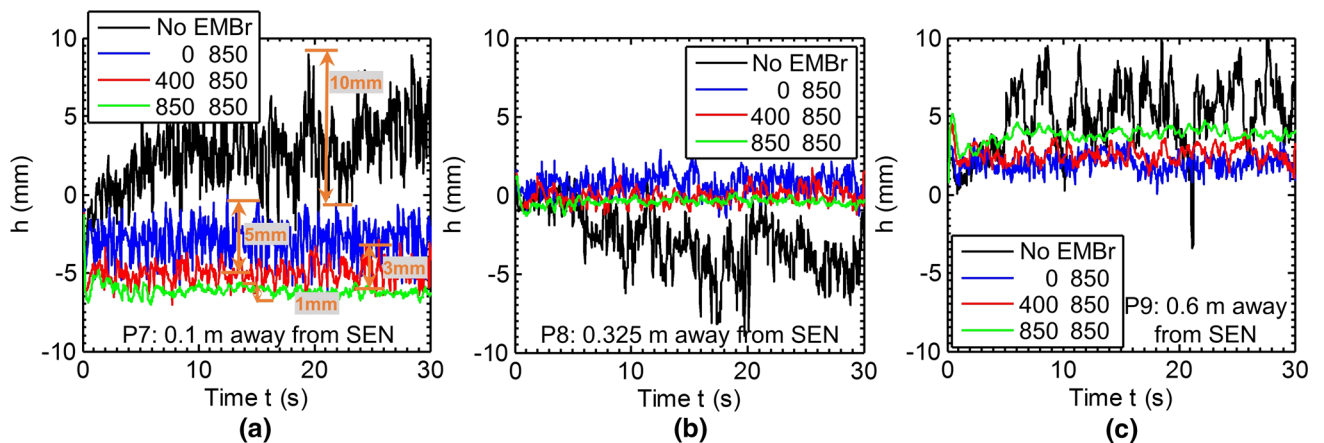


Fig. 27—Surface level history at (a) point P7, (b) point P8, and (c) point P9 with different magnetic field strengths (see Fig. 28 for locations. Legend shows current in top and bottom coils in Amps) (Color figure online).

back-flow region, where flow enters the upper port, are similar to those at  $V_c = 1.3$  m/min. Figures 21(a) and (b) indicate that with zero top coil current, the back-flow region in the port is much smaller. With a top coil current of 850 A, the back-flow region is twice as large. The thinning effect of the EMBr on the jet leads to a larger back-flow region in the port, exceeding one-third of the port area. As the total volume flow rate is constant, the average speed of the steel jet entering the mold must increase with EMBr.

The EMBr affects the flow in SEN, which in turn affects swirl in the SEN bottom and ports. With a submergence depth of 170 mm, increasing the top coil current to 850 A, the maximum magnetic field at the meniscus region reaches  $\sim 0.34$  T, and the swirls almost disappear. Also, for these cases, no significant relation between the top surface velocity and the swirl is seen.

### C. Mold Flow

Figure 22 shows the stream traces superposed with the contours of time-averaged velocity magnitude in the middle center plane of the mold. The well-known double-roll flow pattern is seen for all cases. With EMBr, the circulation regions are closer to the jets, in agreement with previous studies.<sup>[16]</sup> Between the NF and the main recirculation zone that is above the jet, a small counter-rotating circulation region is seen on each side. As EMBr field strength increases, the jets exiting the SEN ports become thinner and stronger.

### D. Surface Flow and Level Fluctuations

As shown earlier, the two jets entering the mold region form classic double-roll recirculation zones. The strength of these recirculation regions strongly affects the top free surface behavior. Figure 23 shows the time-averaged velocity magnitude 1 cm below the top surface for the three cases with EMBr, and the centerline  $x$  velocities ( $\bar{u}_x$ ) are shown in Figure 24. Surface velocity drops from  $\sim 0.4$  m/s with no EMBr to less than 0.07 m/s

for all three EMBR cases, and near the NF the velocity is less than 0.01 m/s. This low surface velocity is inadequate to deliver enough superheat to the meniscus region, thus leading to meniscus solidification, hook formation, and entrapment of slag or inclusion particles.

With EMBr, the top surface velocity profile is much slower and more symmetric about the  $y = 0$  plane. The strong surface velocity and the small secondary vortices near the NF, seen in the case without EMBr, both disappear with EMBr. With top coil current of 850 A, the high-velocity region is slightly larger than with the weaker top magnetic field. The reason is that the jets are thinner and much stronger when the top magnetic field is strong.

Flow across the top surface also affects the surface level profile and its fluctuations. Large surface level fluctuations may cause defects in the product by entraining slag into the molten steel.<sup>[54]</sup> The surface level can be approximated as follows:<sup>[55]</sup>

$$h = \frac{p - p_{\text{mean}}}{\rho g} \quad [11]$$

where  $p_{\text{mean}}$  is the time-averaged pressure along the center line and 1 cm below the top surface, as shown in Figure 25(a). Figure 25(b) shows the surface level profiles calculated using Eq. [11]. Without EMBr, the surface level has a “W” shape with highest surface level of +5 mm near the NF and the lowest level of −3.5 mm at the quarter mold region near P8. When a magnetic field is applied, the surface level profile reverses to a “U” shape. This “U” shape profile has its highest surface level at the NF and lowest level near the SEN. With a stronger magnetic field, the difference,  $\Delta h$ , between the highest and lowest surface levels

increases. Figure 26 shows similar trends with a submergence depth of 200 mm. As expected, increasing the submergence depth reduces the maximum surface level difference. Specifically, without EMBr, increasing submergence depth from 170 to 200 mm reduces  $\Delta h$  from 8 to 5 mm.

Figure 27 shows the time history of the surface level at three typical points: P7, P8, and P9 (with locations given in Figure 25(a)). The standard deviation of the surface level indicates the time-average-level fluctuations and is shown in Table III. Without EMBr, the instantaneous surface level fluctuations can be as large as ~10 mm (see Figure 27(a)). With just the bottom coil current of 850 A, the surface level fluctuations are only ~5 mm near the SEN and 2–3 mm at the quarter mold and NF regions. Further applying the current in the top EMBr ruler coil, the surface level fluctuations drop to ~2 mm. Without EMBr, the average fluctuations are ~2 mm. Increasing the magnetic field strength reduces the level fluctuations. These results quantify how EMBr can be used to lessen the surface level profile variations as well as to reduce the surface level fluctuations.

### E. Turbulent Kinetic Energy

To investigate the effect of EMBr on turbulent flow, the turbulent kinetic energy (TKE) is computed. TKE represents the strength of the turbulence in the flow and can be computed by

$$\text{TKE} = \frac{1}{2} [\langle u_x'^2 \rangle + \langle u_y'^2 \rangle + \langle u_z'^2 \rangle] \quad [12]$$

where  $u_x'$ ,  $u_y'$ , and  $u_z'$  are the fluctuating velocities in the  $x$ ,  $y$ , and  $z$  directions, respectively. The angled brackets imply ensemble averaging in time. Figure 28 shows the predicted TKE in the middle plane of the mold. Since the predicted TKE is roughly symmetric to the  $x = 0$  plane, only half of the middle plane is shown. Without EMBr, the predicted TKE inside the nozzle is ~0.15 m<sup>2</sup>/s<sup>2</sup>, while turning on just the bottom coil reduces the TKE to ~0.1 m<sup>2</sup>/s<sup>2</sup>. After turning on the top coil as well, the predicted TKE inside the nozzle drops to ~0.04 m<sup>2</sup>/s<sup>2</sup>. EMBr dramatically

**Table III. Standard Deviation of Surface Level (mm)**

EMBr Coil Current (A)	Point P7	Point P8	Point P9
No EMBr	1.9	1.5	2.0
$I_{\text{top}} 0 \ I_{\text{bot}} 850$	1.0	0.7	0.6
$I_{\text{top}} 400 \ I_{\text{bot}} 850$	0.6	0.5	0.5
$I_{\text{top}} 850 \ I_{\text{bot}} 850$	0.2	0.2	0.3

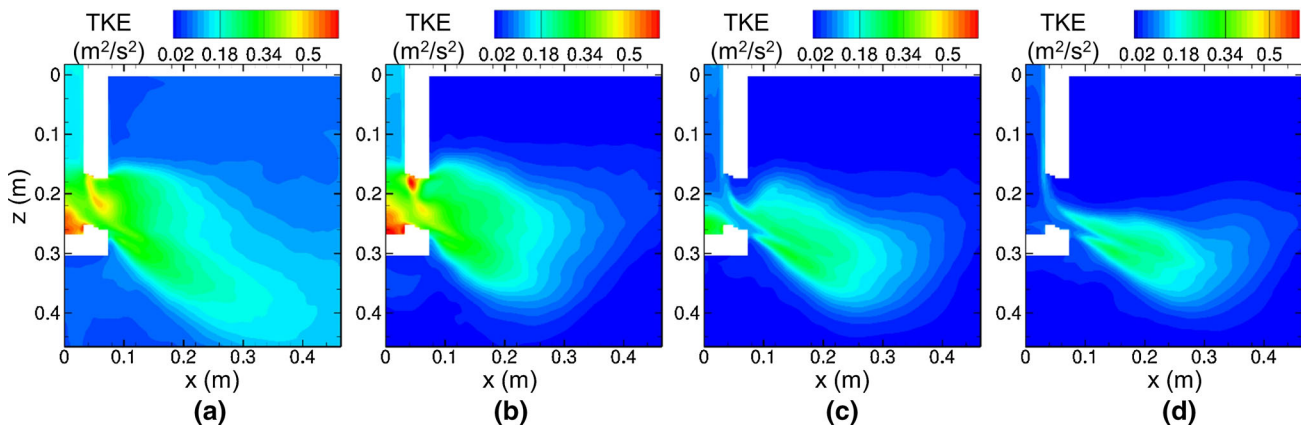


**Fig. 28—Predicted TKE at the middle plane for cases with submergence depth 170 mm and varies magnetic field strengths (a) without EMBr (b) bottom coil current 850 A; (c) top coil 400 A and bottom coil 850 A; (d) both coils 850 A.**



suppresses TKE in the SEN bottom and port exit as well. The high turbulence region around the jet becomes thinner and shorter when EMBR is used. Near the top surface, turning on the bottom EMBR ruler causes the TKE to drop from  $\sim 0.06$  to  $\sim 0.005 \text{ m}^2/\text{s}^2$ . Adding the top ruler further reduces the TKE to  $0.0005 \text{ m}^2/\text{s}^2$ .

## VIII. SUMMARY AND CONCLUSIONS

A multi-GPU-based LES code CUFlow is applied to study the effect of submergence depth and double-ruler EMBR on steel flow in the nozzle and mold region of a typical commercial steel caster. The important findings of this work are summarized below:

1. EMBR causes flow in the nozzle to be more uniform, reducing the extent of asymmetric flow caused by the slide gate. It also increases downward velocity and momentum along the SEN walls, forming an M-shaped velocity profile in the lower part of the SEN.
2. Swirl in the nozzle bottom decreases with increasing casting speed (*via* the accompanying increase in slide gate opening) and with increasing EMBR field strength across the nozzle.
3. Back-flow is often seen in the top portion of the port, or in the core of the big swirl exiting the port. Increasing casting speed from 1.3 to 1.8 m/min has little effect on the size of the back-flow region. EMBR makes the upper back-flow region larger, (occupying more than 1/3 of the port).
4. With EMBR, the jets leaving the ports become thinner and stronger. This is affected by the M-shaped profile inside the SEN and the swirl in the nozzle bottom.
5. When the slide gate moves toward the inner radius side of the nozzle, the time-averaged velocity near the outer radius is higher, although the flow direction is straight toward the SEN without cross flow. Close to the SEN, although the mean velocity is small ( $< 0.1 \text{ m/s}$ ), the transient results have high-velocity ( $\sim 0.4 \text{ m/s}$ ) regions close to the nozzle. With EMBR, the top surface velocity is more uniform with no velocity bias to either side.
6. Without EMBR, vortices form in the corner region close to the NF wall which rotate opposite to the main top recirculation region. These vortices are suppressed with EMBR.
7. Increasing casting speed from 1.5 to 1.8 m/min without EMBR, causes the top surface velocity to exceed  $0.4 \text{ m/s}$ , the surface profile variations to exceed  $10 \text{ mm}$ , and surface level fluctuations of  $\sim 13 \text{ mm}$ , which may cause slag entrainment. These variations are all lowered with EMBR.
8. However, with both EMBR rulers operating in the caster of this study, holding the meniscus level at middle of the top ruler of the EMBR greatly reduces the top surface velocity (to  $\sim 0.05 \text{ m/s}$ ), which may cause inadequate heat transfer at meniscus and may lead to meniscus freezing and slag entrapment.

9. EMBR modifies the top surface level profile from a “W” shape to a “U” shape, lessens its variations, and reduces the turbulence kinetic energy at the top surface.
10. For best steel quality, it is recommended to operate this caster at  $1.8 \text{ m/min}$  with only the bottom EMBR ruler turned on at  $850 \text{ A}$ .

## ACKNOWLEDGMENTS

The authors thank the financial supports from the National Science Foundation (Grant No. CMMI 11-30882) and the Continuous Casting Consortium, Univ. of Illinois at Urbana-Champaign. We also thank Baosteel, Shanghai, P. R. China for providing the measurements and corresponding casting conditions. This research is also part of the Blue Waters sustained-petascale computing project, which is supported by the National Science Foundation (awards OCI-0725070 and ACI-1238993) and the State of Illinois. Blue Waters is a joint effort of the University of Illinois at Urbana-Champaign and its National Center for Supercomputing Applications. The authors also thank NVIDIA Hardware Grant Program for providing the GPUs for an in-house workstation.

## REFERENCES

1. World Steel Association: *World Steel in figures 2014*, World Steel Association, 2014.
2. K. Takatani, K. Nakai, N. Kasai, T. Watanabe, and H. Nakajima: *ISIJ Int.*, 1989, vol. 29, pp. 1063–68.
3. D.-S. Kim, W.-S. Kim, and K.-H. Cho: *ISIJ Int.*, 2000, vol. 40, pp. 670–76.
4. K. Cukierski and B.G. Thomas: *Metall. Mater. Trans. B*, 2008, vol. 39B, pp. 94–107.
5. Y. Haiqi, B. Wang, H. Li, and Jianchao. Li: *J. Mater. Process. Technol.*, 2008, vol. 202, pp. 179–87.
6. Y. Wang and L. Zhang: *Metall. Mater. Trans. B*, 2011, vol. 42B, pp. 1319–51.
7. H. Harada, T. Toh, T. Ishii, K. Kaneko, and E. Takeuchi: *ISIJ Int.*, 2001, vol. 41, pp. 1236–44.
8. Xincheng. Miao, Klaus. Timmel, Dirk. Lucas, Zhongmin. Ren, Sven. Eckert, and Gunter. Gerbeth: *Metall. Mater. Trans. B*, 2012, vol. 43b, pp. 954–72.
9. Z.-D. Qian and W. Yu-Lin: *ISIJ Int.*, 2004, vol. 44, pp. 100–07.
10. Y.-S. Hwang, P.-R. Cha, H.-S. Nam, K.-H. Moon, and J.-K. Yoon: *ISIJ Int.*, 1997, vol. 37, pp. 659–67.
11. R. Singh, B.G. Thomas, and S.P. Vanka: *Metall. Mater. Trans. B*, 2013, vol. 44B, pp. 1201–21.
12. R. Chaudhary, B.G. Thomas, and S.P. Vanka: *Metall. Mater. Trans. B*, 2012, vol. 43, pp. 532–53.
13. Akira. Idogawa, M. Sugizawa, S. Takeuchi, K. Sorimachi, and T. Fujii: *Mater. Sci. Eng. A*, 1993, vol. 173, pp. 293–97.
14. B. Li, T. Okane, and T. Umeda: *Metall. Mater. Trans. B*, 2000, vol. 31B, pp. 1491–503.
15. Y. Miki and S. Takeuchi: *ISIJ Int.*, 2003, vol. 43, pp. 1548–55.
16. R. Singh, B.G. Thomas, and S.P. Vanka: *Metall. Mater. Trans. B*, 2014, vol. 45B, pp. 1098–1115.
17. S.-M. Cho, S.-H. Kim, and B.G. Thomas: *ISIJ Int.*, 2014, vol. 54, pp. 855–64.
18. B. Thomas and Rajneesh Chaudhary: in *6th Int. Conf. Electromagn. Mater. Process. EPM*, Electromagnetic Processing of Materials, Dresden, Germany, 2009, pp. 9–14.
19. J.-E. Eriksson: US Patent US6938674 B2, Sep. 2005.



20. K. Timmel, S. Eckert, G. Gerbeth, F. Stefani, and T. Wondrak: *ISIJ Int.*, 2010, vol. 50, pp. 1134–41.
21. K. Timmel, S. Eckert, and G. Gerbeth: *Metall. Mater. Trans. B*, 2011, vol. 42B, pp. 68–80.
22. R. Chaudhary, C. Ji, B.G. Thomas, and S.P. Vanka: *Metall. Mater. Trans. B*, 2011, vol. 42B, pp. 987–1007.
23. P.H. Dauby: *Rev. Métallurgie*, 2012, vol. 109, pp. 113–36.
24. F. Li, E. Wang, M. Feng, and Z. Li: *ISIJ Int.*, 2015, vol. 55, pp. 814–20.
25. K. Jin, B.G. Thomas, and X. Ruan: *Metall. Mater. Trans. B*, 2016, vol. 47B, pp. 548–65.
26. Q. Yuan: PhD Thesis, University of Illinois at Urbana-Champaign, 2004.
27. R. Liu: PhD Thesis, University of Illinois at Urbana-Champaign, 2015.
28. H. Kobayashi: *Phys. Fluids*, 2005, vol. 17, p. 45104.
29. H. Kobayashi: *Phys. Fluids*, 2008, vol. 20, p. 15102.
30. S.P. Vanka, A.F. Shinn, and K.C. Sahu: in *ASME 2011 Int. Mech. Eng. Congr. Expo.*, American Society of Mechanical Engineers, 2011, pp. 429–37.
31. A.F. Shinn: PhD Thesis, University of Illinois at Urbana-Champaign, 2011.
32. R. Chaudhary: PhD Thesis, University of Illinois at Urbana-Champaign, 2011.
33. P. Kumar, K. Jin, and S.P. Vanka: in *Proc. 1st Therm. Fluids Eng. Summer Conf.*, American Society of Thermal and Fluids Engineers, New York City, August 9, pp. 1–17.
34. S.P. Vanka: *J. Fluids Eng.*, 2013, vol. 135, p. 61401.
35. K. Jin, S.P. Vanka, and B.G. Thomas: *J. Fluids Eng.*, 2015, vol. 137, p. 71104.
36. K. Jin, S.P. Vanka, and R.K. Agarwal: in *52nd AIAA Aerosp. Sci. Meet.*, American Institute of Aeronautics and Astronautics Inc., 2014, pp. 1–16.
37. P. Kumar and S.P. Vanka: *Int. J. Multiph. Flow*, 2015, vol. 77, pp. 32–47.
38. P. Kumar, K. Jin, and S.P. Vanka: in *Proc. 1st Therm. Fluids Eng. Summer Conf.*, American Society of Thermal and Fluids Engineers, New York City, August 9, pp. 1–15.
39. K. Jin, S.P. Vanka, B.G. Thomas, and X.M. Ruan: in *Proc. CFD Model. Simul. Mater. Process.*, The Minerals, Metals & Materials Society, Nashville, Tennessee, 2016, pp. 159–66.
40. S. Yokoya, S. Takagi, S. Ootani, M. Iguchi, K. Marukawa, and S. Hara: *ISIJ Int.*, 2001, vol. 41, pp. 1208–14.
41. S. Garcia-Hernandez, R.D. Morales, J. de Jesús Barreto, and K. Morales-Higa: *ISIJ Int.*, 2013, vol. 53, pp. 1794–1802.
42. S. Yokoya, S. Takagi, M. Iguchi, K. Marukawa, and S. Hara: *ISIJ Int.*, 2001, vol. 41, pp. S47–51.
43. R. Liu, J. Sengupta, D. Crosbie, S. Chung, M. Trinh, and B.G. Thomas: in *Sens. Simul. Process Control*, Wiley, San Diego, 2011, pp. 51–58.
44. R. Liu, B.G. Thomas, J. Sengupta, St.D. Chung, and M. Trinh: *ISIJ Int.*, 2014, vol. 54, pp. 2314–23.
45. J. Kubota, N. Kubo, T. Ishii, M. Suzuki, N. Aramaki, and R. Nishimachi: *NKK Tech. Rev.*, 2001, vol. 85, pp. 1–9.
46. L. Zhang, S. Yang, K. Cai, J. Li, X. Wan, and B.G. Thomas: *Metall. Mater. Trans. B*, 2007, vol. 38B, pp. 63–83.
47. K. Jin, B.G. Thomas, R. Liu, S.P. Vanka, and X.M. Ruan: *IOP Conf. Ser. Mater. Sci. Eng.*, 2015, vol. 84, p. 12095.
48. B.G. Thomas, Q. Yuan, S. Mahmood, R. Liu, and R. Chaudhary: *Metall. Mater. Trans. B*, 2014, vol. 45B, pp. 22–35.
49. J. Kubota, K. Okimoto, A. Shirayama, and H. Mukarami: in *1991 Steelmak. Conf.*, 1991.
50. J. Knoepke, M. Hubbard, J. Kelly, R. Kittridge, and J. Lucas: in *Steelmak. Conf. Proc.*, Iron and Steel Society, Chicago, IL, 1994, pp. 381–88.
51. M. Iguchi, J. Yoshida, T. Shimizu, and Y. Mizuno: *ISIJ Int.*, 2000, vol. 40, pp. 685–91.
52. R.J. Moreau: *Magnetohydrodynamics*, Springer Science & Business Media, Netherlands, 1990.
53. R. Chaudhary, A.F. Shinn, S.P. Vanka, and B.G. Thomas: *Comput Fluids*, 2011, vol. 51, pp. 100–14.
54. L.C. Hibbeler and B.G. Thomas: *Iron Steel Technol.*, 2013, vol. 10, pp. 121–36.
55. R. Chaudhary, B.T. Rietow, and B.G. Thomas: in *Incl. Clean Steels Mater. Sci. Technol. Conf. AISTTMS*, AIST and TMS, Pittsburgh, PA, 2009, pp. 1090–1101.